Germanium as a donor dopant in garnet electrolytes

R.H. Brugge*, J.A. Kilner and A. Aguadero

Department of Materials, Imperial College London, U.K. SW7 2AZ

*Corresponding author: r.brugge14@imperial.ac.uk

Abstract

Cubic $Li_7La_3Zr_2O_{12}$ (LLZO) garnet electrolytes continue to be viewed as an enabler of all-solid-state lithium battery technologies, or as protective membranes for next-generation lithium battery systems. Supervalent dopants at the lithium sublattice are commonly used to stabilise the conductive cubic phase, through the creation of lithium vacancies. The use of germanium (Ge^{4+}) as a higher valent dopant substituting for Li^+ was studied here and shown to stabilise the cubic LLZO phase through substitution of x=0.10 moles of Ge (at the tetrahedral 24*d* Li sites of the space group *Ia*-3*d*, based on the neutron powder diffraction result). This substitution preference follows that of Al^{3+} (having a similar ionic radius and reported to reside at 24*d* sites), but with a lower critical concentration for cubic phase stabilisation, in agreement with charge neutrality arguments to obtain the required Li content (ca. 6.4-6.6 per formula unit) for optimum conductivity. The x=0.10 composition gave the highest bulk Li ion conductivity of $2.8x10^{-4}$ S cm^{-1} at 25 °C, on the order of reported values for Al-doped LLZO. Surface chemical analysis using time of flight secondary ion mass spectrometry showed Ge homogeneously distributed within the grains as well as some Li-, O- and Ge- enrichment along the grain boundaries. Cyclic voltammetry of the cells containing Ge-doped LLZO showed a redox stability up to +5 V.

Keywords: Solid electrolytes, ceramics, ionic conductivity, garnet-type structure, germanium-doped LLZO

Introduction

In the search for a 'next generation' of lithium ion battery technologies, the all-solid-state framework offers an alternative route to conventional liquid-based chemistries, through the possibility of enabling higher energy and power densities by utilising high voltage cathodes and Li metal anodes, as well as significant safety advantages. In particular, the garnet $Li_7La_3Zr_2O_{12}$ (LLZO) is well placed to be used as an electrolyte in such systems, provided the cubic phase is used. Undoped, pure LLZO structure exists as a tetragonal polymorph $I4_1/acd$, which has poor ionic conductivity at room temperature (<10^{-6} S cm^{-1}) due to the ordering of the lithium lattice (full octahedral site occupancy). This space group is the thermodynamically stable form of LLZO, existing at room temperature (RT) due to a volume-preserving tetragonal distortion that relieves internal structural strain [1]. Increasing the temperature to around 650 °C results in a phase transition to the cubic *Ia*-3*d* phase [1–3], which has a disordered Li sublattice (with all Li symmetry sites partially occupied). The cubic phase is the technologically useful form as it has approximately two to three orders of magnitude greater conductivity than the tetragonal phase, and thus stabilising the cubic phase at RT is desired. This is possible through the use of cation supervalent dopants.

Supervalent doping with e.g. Al^{3+} at the Li sublattice introduces Li vacancies (V_{Li}') due to charge balance (Equation 1, in Kröger Vink notation), disrupting the ordering of the Li sublattice to produce the cubic phase [1,4].

$$Al_2O_3 \overset{LLZO}{\Longleftrightarrow} 2Al_{Li}^{\cdot} + 4V_{Li}' + 3O_O^{\times} \qquad (1)$$

These same vacancies are also responsible for opening up previously blocked Li^+ hopping paths leading to an enhanced conductivity. This observation has led to a number of studies focussed on improving the conductivity through doping strategies; these include substitution of donor dopants at the Zr (16*a*) and La (24*c*) sites (i.e. with higher-valent Ta(V) [3,5–10] and Ce(IV) [11]), selected so as to prevent the obstruction of lithium ionic pathways for conduction which might be expected when doping at the Li sites [12]. However, most of the highest RT ionic conductivities in LLZO have actually been achieved by doping on the Li sublattice (with Ga^{3+} and more recently Fe^{3+}) [13–16] , sometimes in combination with a co-dopant at the Zr site [17], suggesting that optimum Li diffusion can be obtained with the Li-substituted dopants, given a particular Li and dopant concentration. The difference in site occupancy behaviours of lithium-substituted dopants and the effect on Li ion diffusivity (and thus conductivity) has been studied [18] , making use of nuclear magnetic resonance (NMR) relaxometry [19]. It was initially believed that the origin of differences in the Li conductivity reported for Al-doped and Ga-doped LLZO lies in the difference site preference for the two dopants – with the larger Ga^{3+} ion occupying the octahedral 96*h* site and Al^{3+} sitting in 24*d* tetrahedra (see Table 2 for a comparison of their effective ionic radii)[12]. The Ga thus might be expected to be less of a hindrance for Li transport, as the 24*d* site is a junction for Li ion diffusion along the 96*h*-24*d*-96*h* Li trajectory, resulting in higher Li ion conductivity. However, difficulties in providing a definitive result for the site occupancy of the dopants and conflicting reports in the literature make this theory difficult to prove, with recent investigations suggesting the change in lattice constant plays a more important role on the Li ion dynamics than the site occupancy of the dopants [18].

It is generally agreed that the optimal Li ion conductivity exists for garnets with a Li content between 6.4 and 6.6 atoms per formula unit (a.p.f.u.) [1,20–24], which corresponds to the lowest number of lithium vacancies required to stabilise the cubic phase. Hence for a trivalent Ga or Al substitution on a Li site, 0.13-0.2 a.p.f.u. of dopant cations are needed. This value provides the guideline for balancing maximum Li content whilst optimising the vacancy content to achieve high conductivity.

Ion	Valence	4 CN effective ionic radius (Å)	6 CN effective ionic radius (Å)
Li	+1	0.59	0.76
Al	+3	0.39	0.535
Ge	+4 (+2)	0.39	0.530 (0.73)
Ga	+3	0.47	0.55

Table 2- Table of effective ionic radii of Li, Al, Ge and Ga cations, showing their valence and effective ionic radii in 4- and 6-fold coordination (CN); data from Shannon's *Revised Effective Ionic Radii.*[25]

Huang *et al.* [26] reported Ge-doped LLZO which stabilised in the cubic phase for ~0.12 Ge a.p.f.u. Using the argument of the optimal Li content of 6.4-6.6 a.p.f.u., and assuming substitution at the Li sublattice, it would be expected that 0.1-0.15 Ge a.p.f.u. would give the best lithium conductivity. They also observed grain growth as a function of Ge content, likening its similarity to Al as a sintering aid. The similarity in ionic radii between Al^{3+} and Ge^{4+} can be seen in Table 2; thus it might be expected that the two cations will have similar crystallographic preferences in the lattice.

In this work, doping with Ge^{4+} was investigated further, using a nominal concentration range of x=0.05 to 0.15 Ge a.p.f.u., with composition $Li_{7-4x}Ge_xLa_3Zr_2O_{12}$ (and abbreviated Gex-LLZO). The effect of this new higher valent dopant on the Li conductivity and electrochemistry, crystal structure and microstructure was carefully investigated by means of electrochemical impedance spectroscopy

(EIS), cyclic voltammetry (CV), neutron and X-ray powder diffraction (NPD and XRD, respectively), scanning electron microscopy (SEM), as well as chemical characterisation by inductively coupled plasma – optical emission spectroscopy (ICP-OES) and time of flight – secondary ion mass spectrometry (TOF-SIMS).

Experimental Section

Synthesis

A series of $Li_{7-4x}Ge_xLa_3Zr_2O_{12}$ compounds with nominal Ge concentrations (x) of 0.05, 0.10, 0.15, 0.30 and 0.50 a.p.f.u were prepared by the modified sol-gel route described previously for Ga-doped LLZO. [13,27] GeO_2 (99.98%), $LiNO_3$ (99%), $La_2(NO_3)_3x6H_2O$ (99.9 %) and Zr(IV) 2,4- pentanedionate $C_{20}H_{28}O_8$ (99.99%) (all Alfa Aesar) were used as reagents and dissolved in citric acid (10 wt%, equivalent to 0.542 M, approx. 200 ml, Sigma Aldrich) and a small amount of nitric acid to aid dissolution (68 wt%, approx. 5-10 ml, VWR Chemicals), with 10 wt% $LiNO_3$ excess added to allow for Li_2O losses during sintering. The resulting solution was heated whilst stirring on a hotplate to form a gel, followed by heating in a combustion furnace (fitted with an exhaust chimney) at 600 °C for 12 hours and held at 100 °C. The combusted powder was milled into a fine powder in an agate mortar and heated to 800 °C for 12 hours in a tube furnace under dry flowing oxygen (99.9999%) with a heat and cool rate of 5 °C min^{-1}. The as-produced powder was cold-pressed into pellets and sintered in an alumina crucible under argon, heating for 6 hours at 1150 °C at a rate of 5 °C min^{-1}. The green pellets were surrounded by a bed of the mother powder to reduce Li_2O loss. All processing steps (milling, pellet forming) were carried out in an argon atmosphere glove box (<0.3 ppm H_2O, <10 ppm O_2) to prevent degradation processes associated with proton-lithium exchange in humid atmosphere[27]. Prior to analysis, pellets of the material were polished with progressively fine SiC grit paper to 4000 grit finish.

Characterisation

ICP-OES: The composition of the pellets was measured by ICP-OES (Thermo Scientific iCAP 6300 Duo). The pellets were crushed and dissolved in 5 wt% nitric acid and calibration standards of Li, La, Zr, Ge and Al (Sigma Aldrich) were produced at 1,5,10 and 20 ppm concentrations.

SEM: SEM investigations were performed with a LEO Gemini 1525 FEGSEM microscope to study the grain size and morphology, using an accelerating voltage of 5 kV. An optical microscope (Nikon Eclipse LV150) was also used. Pellets were thermally etched below their sintering temperature (at 900 °C for 30 minutes in argon) prior to imaging to reveal the grain structure.

XRD: For the preparation of XRD samples, fragments of the sintered pellets were ground in an agate mortar. Pellets were measured with XRD with a Bruker D2 Phaser diffractometer using Cu Kα radiation. Data were collected with the sample spinning in the 2ϑ range 10 ° to 60 °.

NPD: Neutron powder diffraction on the sample with x=0.10 a.p.f.u. were collected at the research reactor at Institut Laue-Langevin (ILL) in France on the D2B high resolution two-axis diffractometer. The sample was sent under argon to prevent reaction with air and moisture. Powder diffraction data were collected at 298 K in constant wavelength mode with λ= 1.594 Å. Data were refined with the FullProf suite program, using Rietveld refinement method.[28]

TOF-SIMS: The chemical homogeneity and phase composition of the polycrystalline pellets was studied using TOF-SIMS (TOF-SIMS V system, ION-TOF GmbH, Munster, Germany), using a 25 kV Bi^+ primary beam for analysis and a 1 kV Cs^+ sputter beam rastered over an area 500 µm by 500 µm, operating under non-interlaced burst alignment mode (using a 1s:1s:1s sputter:wait:analyse cycle). A

low energy electron floodgun was used for charge compensation. The analysed area was 200 µm by 200 µm, and negative secondary ions were detected. Particular regard was given to the spatial distribution of Ge^-. Prior to analysis, pellets were further polished to 0.1 µm using diamond paste and thermally etched (at 900 °C for 30 minutes in argon). Data analysis was carried out with SurfaceLab 6.4 (ION-TOF GmbH) software.

Electrochemical Characterisation

EIS: The ionic conductivity was measured with electrochemical impedance spectroscopy (EIS). Thin films of Au (~50 nm thick, using a 20 mA current for 2 minutes) were sputtered on the top and bottom sides of the pellets which were masked to control the geometry of the Au, to act as ionically blocking electrodes. The Au/LLZO/Au cells were measured under static air using Pt contacts at 298 K and at variable temperatures in a tube furnace as measured by a thermocouple set between 25 and 150 °C. A Solatron 1260 impedance analyser instrument was used, measuring over the frequency range 13 MHz to 1 Hz with a signal amplitude of 100 mV, selected to provide an optimum signal-to-noise ratio whilst maintaining a linear regime between excitation voltage and current response.

CV: The redox stability of Au/Ge0.10-LLZO/Li cells was tested across the voltage range -0.5 V to +5 V vs. Li/Li^+ by CV (Metrohm Autolab NOVA potentiometer) with a scan rate of 1 mV s^{-1}. The working electrode Au was sputtered on one surface of the pellet and a Li electrode acting as both reference electrode and counter electrode was applied to the other side and assembled in a 2032-type coin cell configuration with steel spacers and current collectors in an argon atmosphere glove box.

Results and discussion

XRD patterns of the Ge-doped sintered pellets with a range of nominal Ge content (x) were measured (Figure 1). The sharpest peaks with the material crystallising in the cubic *Ia*-3*d* space group symmetry were found for x=0.10. This is in agreement with the work of Huang[26], in which an optimal dopant concentration of 1 wt% Ge (approximately x=0.12) was suggested for cubic stabilisation. At lower concentrations of Ge (x=0.05), cubic lattice stabilisation is not as effective, resulting in a splitting and broadening of the diffraction peaks, indicative of tetragonal character. For example, the diffraction of the (024) plane in the cubic structure yields one single peak in the theoretical profile, but splits into three peaks in the tetragonal $I4_1/acd$ structure, seen in the x=0.05 pattern. The pattern for x=0.15 is cubic but shows $La_2Zr_2O_7$ impurity peaks, likely to be due to a low initial amount of stoichiometric Li for this composition which is not sufficiently stabilised by Ge^{4+} substituted at the Li sites, preventing the stable formation of the garnet crystal structure. The compositions with x=0.30 and x=0.50 produced XRD patterns containing a large number of impurities, particularly $La_2Zr_2O_7$ and Li_2ZrO_3 (see supplementary Figure S1). No appreciable GeO_2 phases were detected in the XRD patterns at higher concentrations of Ge, which might be expected if a solubility limit is reached in these compositions. This might suggest Ge substitution at the Zr position at these higher concentrations, but was not explored further here. Interestingly this substitution preference at the Zr site was reported by Miara *et al.* by first principles methods[29].

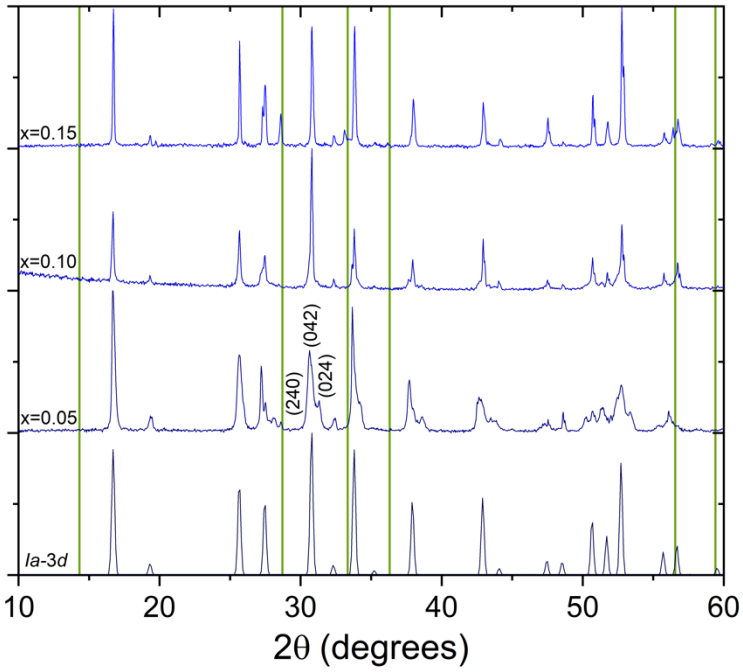

Figure 1. Comparison of pellet XRD patterns of $Li_{7-4x}Ge_xLa_3Zr_2O_{12}$ with x=0.05 (second from bottom), 0.10 and 0.15 (top). A reference pattern for the reflections from the cubic *Ia*-3*d* space group is shown at the bottom. Reflections from the impurity phase $La_2Zr_2O_7$ are marked with green bars. Characteristic splitting of the (024) reflection into (240), (042) and (024) for the tetragonal $I4_1/acd$ distortion is also shown.

Optical and secondary electron images of the pellets show large, well-connected grains – in some cases larger than 100 μm in diameter – and bimodally distributed (Figure 2). No visible pores are seen in the grains, and a geometrically-calculated relative density of the x=0.10 material was calculated as 98 % (using lattice parameters from Rietveld refinement of the neutron diffraction data). In the fracture surface cross-section image (Figure 2b), the fracture surface appears to look smooth, suggesting that the fracture is intergranular in nature and the grain boundaries contain a glassy phase.

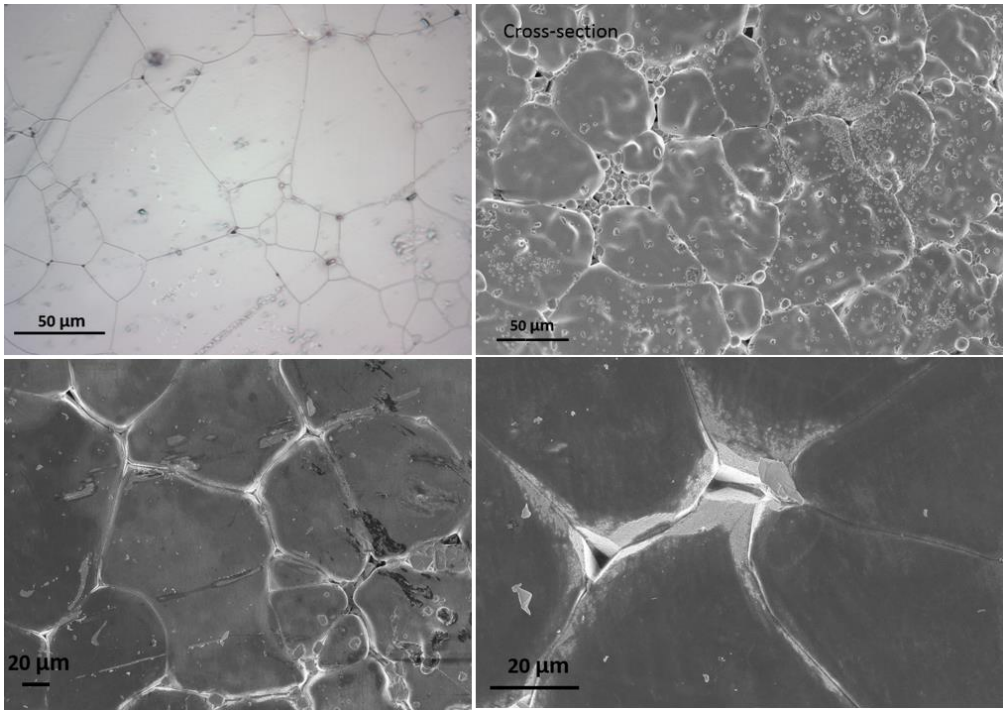

Figure 2- Images of Ge0.10-LLZO pellets, thermally etched at 900 °C. (a) Optical microscope image of surface polished to 1 µm before etching; (b) cross-sectional (fracture surface) optical image and (c, d) surface secondary electron images taken at 5 kV accelerating voltage.

Table 3 shows the measured atomic concentrations given as a.p.f.u. for x=0.05, 0.10 and 0.15 pellet compositions. The Ge content is slightly lower than expected from the nominal stoichiometries of the starting materials (see the final column of Table 3). This may be due to a combination of sub-stoichiometric amounts of Ge being added from the start (through impure reagents and/or human error) and Ge loss during high temperature treatment. Al is present in the samples from being introduced by the alumina crucibles, and is a common impurity found in LLZO materials through the formation of a Li_2O-Al_2O_3 eutectic[30] which forms during the sintering process, as seen by other groups[31–33]. Additionally, Al and Ge appear to exhibit a cooperative effect, in that the aluminium content varies inversely with germanium content, which might be expected if they are competing for the same substitution sites in the lattice as a result of their similar radii [25], and are both acting to stabilise the cubic structure of the material. Introduction of Al at as much as 1.21 wt% was also seen in Huang's initial work on Ge-doped LLZO[34]. The Li content calculated from the total (Ge+Al) concentration, assuming substitution at the Li sublattice, is not the same as the measured content, implying that the dopants are not solely present in the LLZO lattice (but likely also to be found in the grain boundaries, as a result of the liquid phase sintering process). As ICP is a macroscopic technique, differentiation between the composition of grains and grain boundaries is not possible.

Composition (nominal)	Li a.p.f.u.	Ge a.p.f.u.	Al a.p.f.u.	Zr a.p.f.u.	La (fixed) a.p.f.u.	Ge+Al a.p.f.u.	Theoretical Li a.p.f.u. (from Ge+Al content)
Ge0.15-LLZO ($Li_{6.4}Ge_{0.15}La_3Zr_2O_{12}$) x=0.15	6.31	0.12	0	2.01	3	0.12	6.52
Ge0.10-LLZO ($Li_{6.6}Ge_{0.10}La_3Zr_2O_{12}$) x=0.10	6.84	0.05	0.03	2.05	3	0.08	6.71
Ge0.05-LLZO ($Li_{6.8}Ge_{0.05}La_3Zr_2O_{12}$) x=0.05	6.92	0.02	0.13	2.05	3	0.15	6.53

Table 3- ICP-OES measured atomic concentrations for Ge-LLZO pellets with different nominal compositions (x=0.05, 0.10, 0.15).

Chemical analysis using TOF-SIMS mapping showed a distribution of Ge homogeneously across the grains (Figure 3), with a slight enhancement in the Ge^- secondary ion yield at the grain boundaries (which also have an enhancement of Li and O species). This may either correlate with an increase in the sputter rate or ionisation coefficient for these species at the grain boundaries, or an increase in the concentration compared to the grains (or a combination of these factors), but it is not possible to be definitive about the origin of the enhancement. However, the formation of a Li_2O-GeO_2 eutectic at temperatures below the sintering temperature (of which there are several)[35] may explain the observed large grains and Ge present at the grain boundaries, which was also observed by Huang, particularly at higher doping contents of Ge[26]. It is known, for example, that grain growth in Al-doped LLZO is aided by the formation of the Li_2O-Al_2O_3 liquid eutectic during sintering[30].

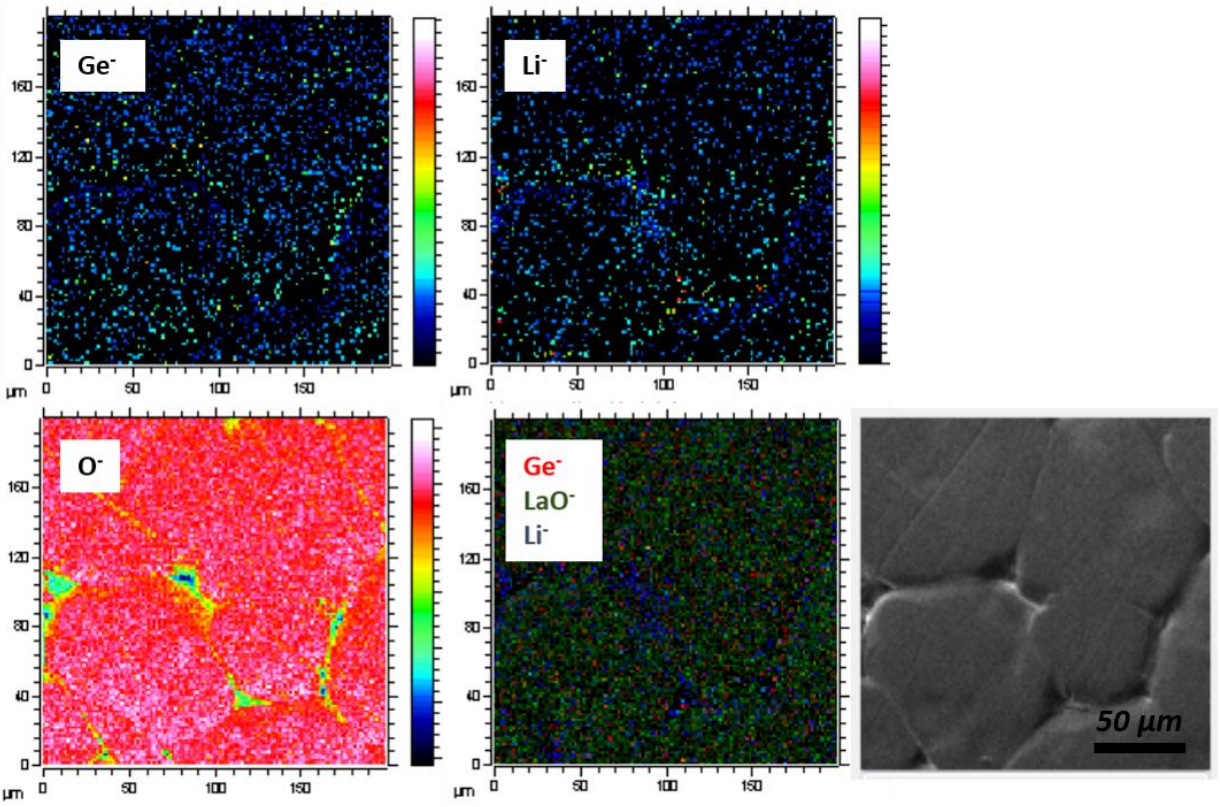

Figure 3. TOF-SIMS maps of the surface of a Ge0.10-LLZO (x=0.10) pellet (optical image shown on the far right), showing $^{74}Ge^-$, $^{7}Li^-$ and $^{16}O^-$ secondary ion maps of counts of selected species over total ion counts and an overlay of $^{74}Ge^-$, $^{155}(LaO)^-$ and $^{7}Li^-$ species (in red, green and blue, respectively). Maps were taken with a Bi^+ primary ion beam (25 kV, 0.2 pA) and a Cs^+ sputter gun (1 kV, 64 nA) operated in non-interlaced burst alignment mode (using a 1s:1s:1s sputter:wait:analyse cycle).

Room temperature impedance spectra of the Ge-LLZO pellets with symmetric Au electrodes for the compositions x=0.05, 0.10 and 0.15 are shown in Figure 4. The spectra show a high frequency semicircle followed by a low frequency contribution coming from the highly resistive electrodes. The presence of an additional arc due to grain boundaries or interface effects is not clearly seen by eye in the spectra, and may be hidden in the electrode response. To quantify the spectra, combinations of a resistor in parallel with a constant phase element (denoted R//CPE) are used, with a high frequency inductance *L* (on the order 10^{-6} H) and an internal resistance R_{int} fixed at 5 Ω (measured with a blank, or 'shorted' cell) in series. The feature at 1 MHz in which a discontinuity of the data points is seen is due to an instrumental artefact, caused by a mismatch of the input and output signals in the frequency response analyser.

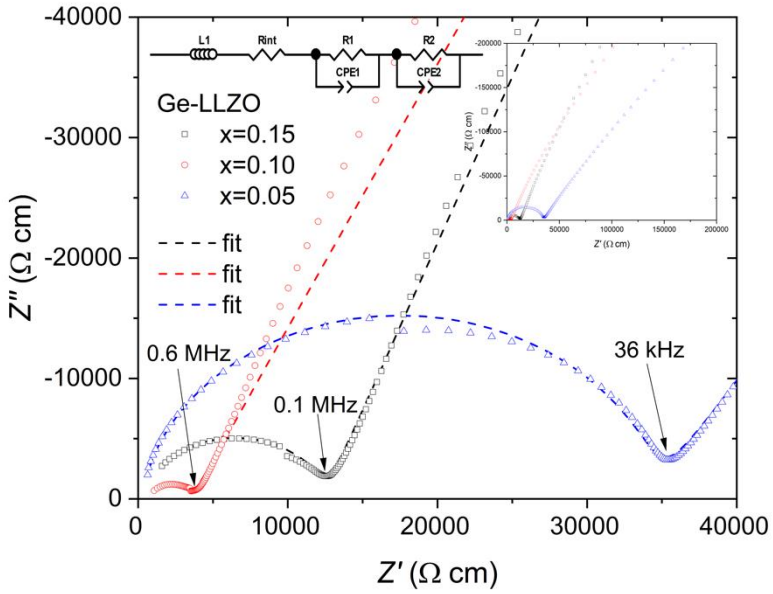

Figure 4- Nyquist plots of impedance spectra of Ge0.15-, Ge0.10- and Ge0.05-LLZO pellets with symmetrical Au electrodes measured at 298 K across the frequency range 13MHz to 1 Hz. The inset shows low frequency data points.

The high frequency semicircle is fitted to a single R1//CPE1 component, describing a resistor (with resistance R_1) and constant phase element (CPE_1) in parallel. The conductivity σ corresponding to the high frequency component was calculated from *R* and Equation 2, where *l* is the electrolyte thickness and *A* is the electrode area.

$$\sigma = \frac{l}{R\ A} \qquad (2)$$

The capacitance is calculated from the constant phase element fit, where:

$$Z_{CPE} = \frac{1}{Q(i\omega)^n} \quad (3)$$

Here, ω is the angular frequency, n is the description of non-ideality, Q is the non-ideal capacitance, and C is found from Equation 4[36]:

$$C=(R^{1-n}Q)^{1/n} \quad (4)$$

The relative permittivity, ε_r, is calculated from the capacitance C by Equation 5, where ε_0 is the vacuum permittivity (8.854x10^{-14} F/cm): [37]

$$\varepsilon_r = \frac{Cl}{A\varepsilon_0} \quad (5)$$

	Ge0.05-LLZO	Ge0.10-LLZO	Ge0.15-LLZO
R (Ohms)	17236	1149	4747
σ_{bulk} (S cm-1)	2.91x10^{-5}	2.80x10^{-4}	8.05x10^{-5}
CPE (F s^{n-1})	3.5x10^{-11}	2.3 x10^{-10}	1.3 x10^{-10}
n	0.94	0.86	0.87
C (F)	1.47 x10^{-11}	1.82 x10^{-11}	1.43 x10^{-11}
C *l/A (F cm^{-1})	7.40 x10^{-12}	5.87 x10^{-12}	5.45 x10^{-12}
ε_r	88	66	62

Table 4 – calculated values of conductivity, σ, capacity, C, and relative permittivity, ε_r, from the high-frequency component fit to a single R//CPE element in Figure 4 Nyquist plots, taken at 298 K. l is the pellet thickness, A the electrode area, and n the non-ideality factor for capacitance.

The fitting of the high frequency arc supports the resistance R_1 indicative of a bulk transport process as the parallel geometric capacitance values are in the pF range [38], and the calculated relative permittivity (ε_r) values are of the order of 60-80. These values are in the range of bulk permittivity for oxides and garnets reported in the literature [14,39]. Accordingly, the values of bulk conductivity, σ_{bulk}, of Li in the Ge-LLZO samples are of the order 10^{-4} S/cm, with the highest value found for the x=10 (Ge0.10-LLZO) composition. The bulk conductivity is slightly lower than the total conductivity reported by Huang *et al.* [26] (8.28x10^{-4} S cm^{-1}), but on a par with some Al-doped LLZO materials reported in the literature[39,40]. Differences in the microstructure between these samples and the samples in Huang's report are difficult to compare due to a lack of clear micrographs in the latter; however, the role of grain boundaries on the fitting and reporting of bulk, grain boundary and total conductivities is likely to be significant. As is often the case in these materials, the grain boundary contribution to the ionic transport is not definitive using impedance analysis, as it is often hidden in the bulk or electrode response, making separation of bulk and grain boundary resistances difficult. The comparatively low values (by approximately one order of magnitude) of bulk conductivity in the Ge-LLZO samples here versus Ga-doped LLZO reported in the literature [13–16,27] implies that the role of the dopant on the transport properties differs for Ga and Ge substitution. This may be due to a combination of differences in crystallographic site preference, and segregation of dopants at grain boundaries, leading to differences in the grain boundary resistance. For example, we have reported previously a clear Al segregation at grain boundaries in Al-LLZO, but a more homogeneous distribution of Ga in Ga-LLZO[41], leading to a marked difference in the critical current density for cell failure resulting from Li dendrite formation (which form along the grain boundaries) in symmetric cells of these two materials.

Variable temperature impedance measurements were carried out on the Ge0.10-LLZO sample. The high frequency bulk arc remains largely unchanged following the heating treatment, as seen in its Arrhenius plot (Figure 5). The bulk data at variable temperature (R1//CPE1 element, high frequency arc) gave capacitances from CPE_1 of the order of 10^{-12} F with very little variance (with a standard deviation of $4.2x10^{-12}$ F across the temperature range measured), and values of relative permittivity are in the range 50-70 except at the higher temperatures (above 90 °C, where the fit is less accurate owing to loss of data points in the high frequency arc); see supplementary Table S2. The Arrhenius fit (to σT) gives a bulk RT conductivity of $4.2x10^{-5}$ S cm^{-1} for the material and the activation energy of 0.38 eV is in good agreement with literature values for bulk conductivity in Al-doped LLZO garnets [7,42–44].

Heating to higher temperatures resulted in an intermediate frequency feature becoming more pronounced, which could be separated from the low frequency tail of the electrode response at the higher temperatures (Figure S2). A detailed analysis of this component is not attempted here, in part owing to complications in the fit and because the experiments were carried out in air, making degradation processes at the surface and grain boundaries likely. It was noted that attempting to fit the intermediate frequency arc to an R//CPE element gave *n* values for the CPE below 0.50 above 90 °C, making quantification challenging (see Table S3).

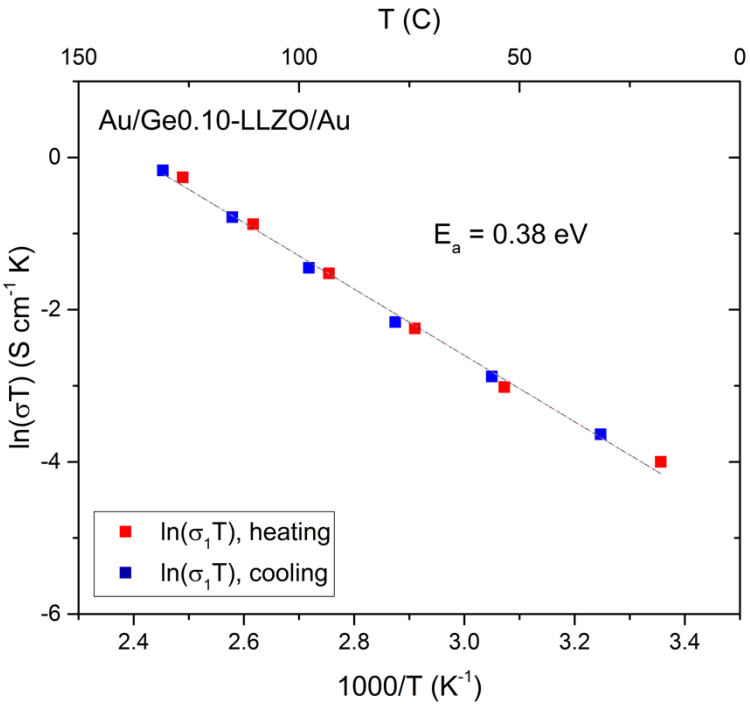

Figure 5- Arrhenius plot of the high frequency (σ_1) arc fit of the impedance spectra for Ge0.10-LLZO with gold sputtered electrodes using the equivalent circuit model shown in Figure 4, on heating and cooling.

The x=0.10 composition was used for the NPD study as it was the best composition for stabilising the desired cubic phase. The powder was prepared by calcining in the normal way (800 °C in oxygen), followed by thermal treatment of the resulting powder at 1150 °C in argon (as used for sintering, but without pressing into a pellet). Rietveld refinement of the pattern shown in Figure 6 and Table 6 suggested that the Ge^{4+} substitutes for Li^+ at the 24*d* tetrahedral site, giving a best fit for this site when the concentration was fixed at 0.10 Ge a.p.f.u. The Ge atoms were allowed to be refined at

both Li1 and Li2 sites, but this led to a preferential occupancy of the Li1 (24*d*) site only. Refining at the Zr site yielded unfavourable occupancies of Zr and Ge (too high), and preferential occupancy of the Li1 site when it was allowed to be refined together with the Zr site for Ge occupancy.

The possibility of Al doping in the crystalline phase was investigated by attempting refinement of Al in both Li1 and Li2 sites, but this lead to negative values of B_{iso} and no improvement in reliability factors. Given the low amount of Al expected in the sample from ICP results (0.03 a.p.f.u.), and the likelihood of it existing in an amorphous phase along the grain boundaries of the sample (which is not as likely to exist in the 'sintered' powder used for the NPD analysis), we are not able to quantitatively determine the amount of Al in the crystal structure here.

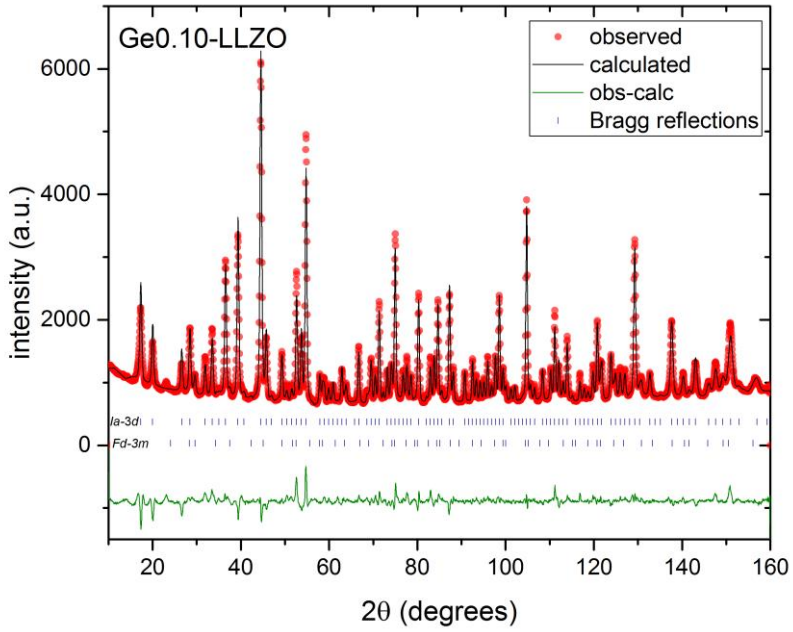

Figure 6- NPD pattern with Rietveld refinement, showing observed, calculated and difference (obs-calc) patterns fitting to *Ia*-3*d* space group and pyrochlore $La_2Zr_2O_7$ impurity (space group *Fd*-3*m*), occupying 5.79 wt% of the total (with the Bragg reflections shown as short vertical lines).

Species	**Site**	***x/a, y/b, z/c***	***B*iso**	**Occupancy**
Li1	24*d*	0.375,0,0.25	2.58(5)	2.83(2)
Li2	96*h*	0.0997(2), 0.6865(2), 0.5770(2)	0.500	3.78(2)
La	24*c*	0.125, 0, 0.25	0.748(6)	3.000
Zr	16*a*	0, 0, 0	0.724(6)	2.000
Ge	24*d*	0.375,0,0.25	2.58(5)	0.100
O	96*h*	-0.03226(2), 0.05363(2), 0.14945(2)	1.142(6)	12.000

Table 6- NPD data of Ge0.10-LLZO determined by Rietveld refinement. Space group: *Ia*-3*d* (no. 230); lattice parameter: $a = b = c = 12.963\ 5(1)$ Å. *R*-factors: *R* = 7:91, $\chi^2 = 12.9$. B_{iso} is the isotropic atomic displacement parameter; the constraint on this parameter is such that B_{iso} (Li1) = B_{iso} (Ge). The density of the Ge0.10-LLZO powder phase is refined as 5.143 g cm^{-3}.

The EIS and NPD findings support the view that occupancy of 24*d* Li sites by aliovalent dopants (as seen with Al^{3+} and in some literature reports, Ga^{3+}) can enhance the lithium conductivity of LLZO. Using the higher valent dopant Ge^{4+} enables the stabilisation of the cubic phase with a lower dopant content than when cations with lower oxidation states are used. However, Ge0.10-LLZO is not able to provide the highest values of conductivity reported for some Ga-LLZO compositions, suggesting site blocking arguments on the lithium sublattice do not tell the whole story. Further verification of Ge site occupancy through ^{73}Ge nuclear magnetic resonance (NMR), was not attempted here as this NMR active nucleus has a low natural abundance (7.8 %) a small gyromagnetic ratio and spin 9/2, complicating line shape analysis.

Finally, the electrochemical stability of Ge-doped LLZO was tested by a CV experiment on a Li/Ge0.10-LLZO/Au cell to measure the electrochemical window of the pellet. As seen in Figure 8, a set of lithium stripping (positive current) and deposition (negative current) peaks are seen either side of the 0 V point, and an additional peak attributed to the Au-Li alloying reaction is seen at ca. 1.5 V, but no other redox peaks can be seen at higher voltages up to +5 V, indicating the stability of Ge0.10-LLZO against redox processes in the presence of Li metal and a lack of degradation reactions involving Li^+ ions.

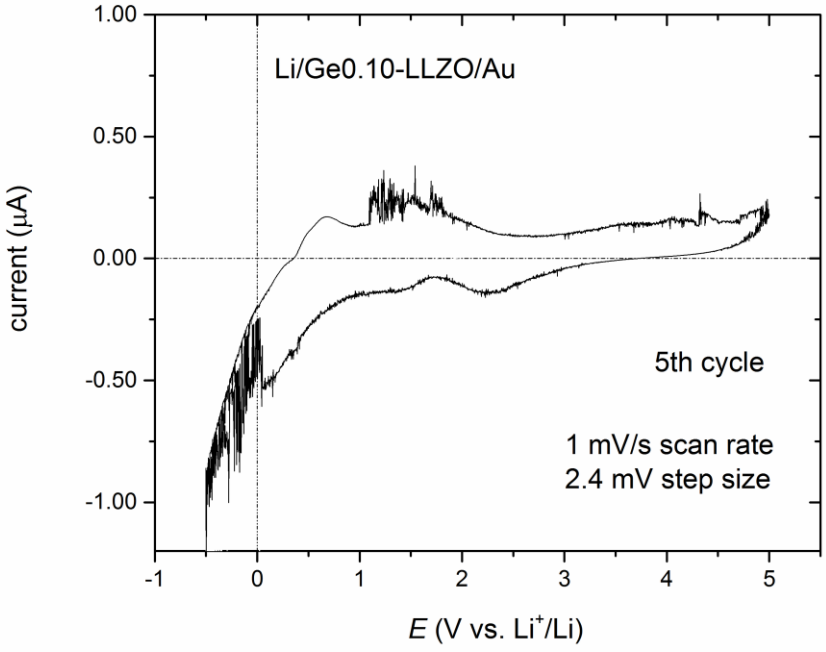

Figure 8- Cyclic voltammogram of Li/Ge0.10-LLZO/Au cell in the potential range from -0.5 V to +5 V vs. Li/Li^+.

Conclusion

Germanium has been shown to be effective as a dopant in stabilising the cubic phase and providing an enhancement in conductivity in garnet LLZO electrolytes. About 0.10 Ge^{4+} is enough to stabilise the cubic phase to give the critical Li content of 6.6 Li a.p.f.u., providing bulk conductivities up to 2.8×10^{-4} S cm^{-1} at 25 °C. Higher Ge contents (above 0.15 Ge a.p.f.u.) resulted in the formation of impurity phases. Ge^{4+} has a similar ionic radius to Al^{3+} which is known to substitute at the Li site and stabilise the cubic phase; ICP-OES showed a cooperative effect between Al and Ge cations in entering the Ge-LLZO pellets for compositions with a range of Ge content. NPD refinement suggests

that Ge substitutes at the Li 24*d* site, in similarity to Al^{3+} reported in Al-LLZO. Chemical analysis showed a homogeneous Ge distribution in the grains and some enrichment at the grain boundaries, possibly due to the presence of a GeO_2-Li_2O eutectic during high temperature sintering, which aids grain growth and densification of the pellets, akin to the well-known alumina eutectic in Al-containing samples sintered in alumina crucibles. The Ge-LLZO electrolyte cell was redox stable against lithium metal under a large operational voltage range up to +5 V vs. Li/Li^+.

References

1. Bernstein, N., Johannes, M. D. & Hoang, K. Origin of the structural phase transition in $Li_7La_3Zr_2O_{12}$. *Phys. Rev. Lett.* **109,** 1–5 (2012).

2. Larraz, G., Orera, A. & Sanjuán, M. L. Cubic phases of garnet-type $Li_7La_3Zr_2O_{12}$: the role of hydration. *J. Mater. Chem. A* **1,** 11419–11428 (2013).

3. Wang, Y. & Lai, W. Phase transition in lithium garnet oxide ionic conductors $Li_7La_3Zr_2O_{12}$: The role of Ta substitution and H_2O/CO_2 exposure. *J. Power Sources* **275,** 612–620 (2015).

4. Mukhopadhyay, S., Thompson, T., Sakamoto, J. Huq, A., Wolfenstine, J., Allen, J. L., Bernstein, N., Stewart, D. A. & Johannes, M. D. Structure and stoichiometry in supervalent doped $Li_7La_3Zr_2O_{12}$. C*hem. Mater.* **27,** 3658–3665 (2015).

5. Adams, S. & Rao, R. P. Ion transport and phase transition in $Li_{7-x}La_3(Zr_{2-x}M_x)O_{12}$ (M = Ta^{5+}, Nb^{5+}, x = 0, 0.25). *J. Mater. Chem.* **22,** 1426–1434 (2012).

6. Gu, W., Ezbiri, M., Rao, R. P., Avdeev, M. & Adams, S. Effects of penta-and trivalent dopants on structure and conductivity of $Li_7La_3Zr_2O_{12}$. *Solid State Ionics* **274,** 100–105 (2015).

7. Li, Y., Han, J.-T., Wang, C.-A., Xie, H. & Goodenough, J. B. Optimizing Li^+ conductivity in a garnet framework. *J. Mater. Chem.* **22,** 15357 (2012).

8. Miara, L. J., Ong S. P., Mo, Y., Richards, W. D., Park, Y., Lee, J.-M., Lee, H. S. & Ceder, G. Effect of Rb and Ta Doping on the Ionic Conductivity and Stability of the Garnet $Li_{7+2x-y}(La_{3-x}Rb_x)(Zr_{2-y}Ta_y)O_{12}$ ($0 \le x \le 0.375$, $0 \le y \le 1$) Superionic Conductor: A First Principles Investigation. *Chem. Mater.* **25,** 3048–3055 (2013).

9. Tsai, C.-L., Roddatis, V., Chandran, C. V., Ma, Q., Uhlenbruck, S., Bram, M., Heitjans, P. & Guillon, O. $Li_7La_3Zr_2O_{12}$ Interface Modification for Li Dendrite Prevention. *ACS Appl. Mater. Interfaces* **8,** 10617–10628 (2016).

10. Yow, Z. F., Oh, Y. L., Gu, W., Rao, R. P. & Adams, S. Effect of Li^+/H^+ exchange in water treated Ta-doped $Li_7La_3Zr_2O_{12}$. *Solid State Ionics* **292,** 122–129 (2016).

11. Rangasamy, E., Wolfenstine, J., Allen, J. L. & Sakamoto, J. The effect of 24c-site (A) cation substitution on the tetragonal-cubic phase transition in $Li_{7-x}La_{3-x}A_xZr_2O_{12}$ garnet-based ceramic electrolyte. *J. Power Sources* **230,** 261–266 (2013).

12. Allen, J. L., Wolfenstine, J., Rangasamy, E. & Sakamoto, J. Effect of substitution (Ta, Al, Ga) on the conductivity of $Li_7La_3Zr_2O_{12}$. *J. Power Sources* **206,** 315–319 (2012).

13. Bernuy-Lopez, C., Manalastas, W., Lopez del Amo, J. M., Aguadero, A., Aguesse, F. & Kilner, J. A. Atmosphere Controlled Processing of Ga-Substituted Garnets for High Li-Ion Conductivity Ceramics. *Chem. Mater.* **26,** 3610–3617 (2014).

14. Rettenwander, D., Redhammer, G., Preishuber-Pflügl, F., Cheng, L., Miara, L., Wagner, R., Welzl, A., Suard, E., Doeff, M. M., Wilkening, M., Fleig, J. & Amthauer, G. Structural and Electrochemical Consequences of Al and Ga Cosubstitution in $Li_7La_3Zr_2O_{12}$ Solid Electrolytes.

Chem. Mater. **28,** 2384–2392 (2016).

15. Wagner, R., Redhammer, G. J., Rettenwander, D., Tippelt, G., Welzl, A., Taibl, S., Fleig, S., Franz, A., Lottermoser, W. & Amthauer, G. Fast Li-ion conducting garnet-related $Li_{7-3x}Fe_xLa_3Zr_2O_{12}$ with uncommon I-43d structure. *Chem. Mater.* **28,** 5943-5951 (2016).

16. Wu, J.-F. Chen, E.-Y., Yu, Y., Liu, L., Wu, Y., Pang, W. K., Peterson, V. K. & Guo, X. Gallium-doped $Li_7La_3Zr_2O_{12}$ garnet-type electrolytes with high lithium-ion conductivity. *ACS Appl. Mater. Interfaces* **9,** 1542–1552 (2017).

17. Buannic, L. Orayech, B., Lopez del Amo, J.-M., Carrasco, J., Katcho, N. A., Aguesse, F., Manalastas, W., Zhang, W., Kilner, J. A. & Llordes, A. Dual Substitution Strategy to Enhance Li+ Ionic Conductivity in $Li_7La_3Zr_2O_{12}$ Solid Electrolyte. *Chem. Mater.* **29,** 1769–1778 (2017).

18. Rettenwander, D., Langer, J., Schmidt, W., Arrer, C., Harris, K. J., Terskikh, V., Goward, G. G., Wilkening, M. & Amthauer, G. Site occupation of Ga and Al in stabilized cubic $Li_{7-3(x+y)}Ga_xAl_yLa_3Zr_2O_{12}$ garnets as deduced from ^{27}Al and ^{71}Ga MAS NMR at ultrahigh magnetic fields. *Chem. Mater.* **27,** 3135–3142 (2015).

19. Bottke, P., Rettenwander, D., Schmidt, W., Amthauer, G. & Wilkening, M. Ion Dynamics in Solid Electrolytes: NMR Reveals the Elementary Steps of Li^+ Hopping in the Garnet $Li_{6.5}La_3Zr_{1.75}Mo_{0.25}O_{12}$. *Chem. Mater.* **27,** 6571–6582 (2015).

20. Kihira, Y., Ohta, S., Imagawa, H. & Asaoka, T. Effect of Simultaneous Substitution of Alkali Earth Metals and Nb in $Li_7La_3Zr_2O_{12}$ on Lithium-Ion Conductivity. *ECS Electrochem. Lett.* **2,** A56–A59 (2013).

21. Nozaki, H., Harada, M., Ohta, S., Watanabe, I., Miyake, Y., Ikedo, Y., Jalarvo, N. H., Mamontov, E. & Sugiyama, J. Li diffusive behavior of garnet-type oxides studied by muon-spin relaxation and QENS. *Solid State Ionics* **262,** 585–588 (2014).

22. Thompson, T., Sharafi, A., Johannes, M. D., Huq, A., Allen, J. L., Wolfenstine, J. & Sakamoto, J. A Tale of Two Sites: On Defining the Carrier Concentration in Garnet-Based Ionic Conductors for Advanced Li Batteries. *Adv. Energy Mater.* **5,** 1500096 (2015).

23. Xie, H., Alonso, J. A., Li, Y., Fern, M. T. & Goodenough, J. B. Lithium Distribution in Aluminum-Free Cubic $Li_7La_3Zr_2O_{12}$. *Chem. Mater.* **23,** 3587–3589 (2011).

24. Jalem, R., Rushton, M. J. D., Manalastas, W., Nakayama, M., Kasuga, T., Kilner, J. A. & Grimes, R. W. Effects of Gallium Doping in Garnet-Type $Li_7La_3Zr_2O_{12}$ Solid Electrolytes. *Chem. Mater.* **27,** 2821–2831 (2015).

25. Shannon, R. D. Revised Effective Ionic Radii and Systematic Studies of Interatomic Distances in Halides and Chalcogenides. *Acta Crystallogr. A* **32,** 751–767 (1976).

26. Huang, M., Xu, W., Shen, Y., Lin, Y.-H. & Nan, C.-W. X-ray absorption near-edge spectroscopy study on Ge-doped $Li_7La_3Zr_2O_{12}$: enhanced ionic conductivity and defect chemistry. *Electrochim. Acta* **115,** 581–586 (2014).

27. Brugge, R. H., Hekselman, A. K. O., Cavallaro, A., Pesci, F. M., Chater, R. J. Kilner, J. A. & Aguadero, A. Garnet Electrolytes for Solid State Batteries: Visualisation of Moisture-Induced Chemical Degradation and Revealing its Impact on the Li-Ion Dynamics. *Chem. Mater.* **30,** 3704–3713 (2018).

28. Rodríguez-Carvajal, J. Recent advances in magnetic structure determination by neutron powder diffraction. *Phys. B Condens. Matter* **192,** 55–69 (1993).

29. Miara, L. J., Richards, W. D., Wang, Y. E. & Ceder, G. First-principles studies on stable cation

dopants and electrolyte|cathode interfaces for garnet $Li_7La_3Zr_2O_{12}$. *Chem. Mater.* **27,** 4040-4047 (2015).

30. Cook, L. P. & Plante, E. R. Phase Diagram of the System Li_2O-Al_2O_3. *Ceram. Trans.* **83,** (1992).

31. Murugan, R., Thangadurai, V. & Weppner, W. Fast lithium ion conduction in garnet-type $Li_7La_3Zr_2O_{12}$. *Angew. Chemie - Int. Ed.* **46,** 7778–7781 (2007).

32. Ahn, J. H., Park, S. Y., Lee, J. M., Park, Y. & Lee, J. H. Local impedance spectroscopic and microstructural analyses of Al-in-diffused $Li_7La_3Zr_2O_{12}$. *J. Power Sources* **254,** 287–292 (2014).

33. Kumazaki, S., Iriyama, Y., Kim, K.-H., Murugan, R., Tanabe, K., Yamamoto, K., Hirayama, T. & Ogumi, Z. High lithium ion conductive $Li_7La_3Zr_2O_{12}$ by inclusion of both Al and Si. *Electrochem. commun.* **13,** 509–512 (2011).

34. Huang, M., Dumon, A. & Nan, C.-W. Effect of Si, In and Ge doping on high ionic conductivity of $Li_7La_3Zr_2O_{12}$. *Electrochem. commun.* **21,** 62–64 (2012).

35. Murthy, M. K. & Ip, J. Studies in Germanium Oxide Systems : I, Phase Equilibria in the System Li_2O-GeO_2. *J. Am. Chem. Soc.* **47,** 328–331 (1964).

36. Fleig, J. The grain boundary impedance of random microstructures: Numerical simulations and implications for the analysis of experimental data. *Solid State Ionics* **150,** 181–193 (2002).

37. Bron, P., Roling, B. & Dehnen, S. Impedance characterization reveals mixed conducting interphases between sulfidic superionic conductors and lithium metal electrodes. *J. Power Sources* **352,** 127–134 (2017).

38. Irvine, J. T. S., Sinclair, D. C. & West, A. R. Electroceramics Characterization by Impedance Spectroscopy. *Adv. Mater.* **2,** 132–138 (1990).

39. Wachter-Welzl, A., Kirowitz, J., Wagner, R., Smetaczek, S., Brunauer, G. C., Bonta, M., Rettenwander, D., Taibl, S., Limbeck, A., Amthauer, G. & Fleig, J. The origin of conductivity variations in Al-stabilized $Li_7La_3Zr_2O_{12}$ ceramics. *Solid State Ionics* **319,** 203–208 (2018).

40. Buschmann, H., Dolle, J., Berendts, S., Kuhn, A., Bottke, P., Wilkening, M., Heitjans, P., Senyshyn, A., Ehrenberg, H., Lotnyk, A., Duppel, V., Kienle, L. & Janek, J. Structure and dynamics of the fast lithium ion conductor '$Li_7La_3Zr_2O_{12}$'. *Phys. Chem. Chem. Phys.* **13,** 19378–92 (2011).

41. Pesci, F. M., Brugge, R. H., Hekselman, A. K. O., Cavallaro, A., Chater, R. J. & Aguadero, A. Elucidating the Role of Dopants on the Critical Current Density for Dendrites Formation in Garnet Electrolytes. *J. Mater. Chem. A* **6,** 19817-19827 (2018).

42. Jin, Y. & McGinn, P. J. Al-doped $Li_7La_3Zr_2O_{12}$ synthesized by a polymerized complex method. *J. Power Sources* **196,** 8683–8687 (2011).

43. Sudo, R., Nakata, K., Ishiguro, K., Matsui, M., Hirano, A., Takedo, Y., Yamamoto, O. & Imanishi, N. Interface behavior between garnet-type lithium-conducting solid electrolyte and lithium metal. *Solid State Ionics* **262,** 151–154 (2014).

44. Suzuki, Y., Kami, K., Watanabe, K. & Imanishi, N. Characteristics of discharge products in all-solid-state Li-air batteries. *Solid State Ionics* **278,** 222–227 (2015).

Conflicts of interest

The authors declare no conflicts of interest.

Acknowledgements

The authors wish to thank Maria Teresa Fernandez-Diaz at ILL for the neutron diffraction measurement. This work was funded by an EPSRC grant (EP/R024006/1) and PhD studentship.